Theory-guided synthesis of a 2D tungsten titanium MXene from a covalently bonded layered carbide for electrocatalysis

Anupma Thakur[1,2,3], Wyatt J. Highland[2,3], Brian C. Wyatt[2,3], Jiayi Xu[4], Nithin Chandran B.S.[1,2,3], Bowen Zhang[2,3], Zachary D. Hood[5], Shiba P. Adhikari[5], Emad Oveisi[6], Barbara Pacakova[7], Fernando Vega[8], Jeffrey Simon[9], Colton Fruhling[9], Benjamin Reigle[9], Mohammad Asadi[10], Vladimir Shalaev[9], Alexandra Boltasseva[9], Thomas E. Beechem[8], Cong Liu[4], Babak Anasori[1,2,3,8*]

[1]School of Materials Engineering, Purdue University, West Lafayette, Indiana 47907, United States

[2]Department of Mechanical and Energy Engineering, Purdue School of Engineering and Technology, Indiana University-Purdue University Indianapolis, Indianapolis, IN, 46202 USA

[3]Integrated Nanosystems Development Institute, Indiana University-Purdue University Indianapolis, Indianapolis, IN, 46202 USA

[4]Chemical Sciences and Engineering Division, Argonne National Laboratory, Lemont, IL 60439, USA

[5]Applied Materials Division, Argonne National Laboratory, Lemont, Illinois 60439, United States

[6]Interdisciplinary Center for Electron Microscopy, École Polytechnique Fédérale de Lausanne, CH-1015 Lausanne, Switzerland
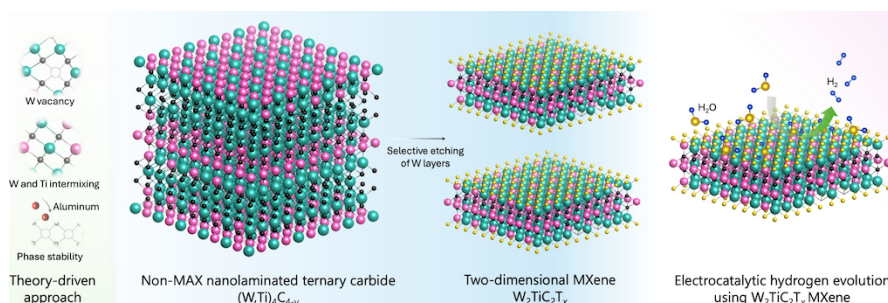
[7]Department of Physics, Norwegian University of Science and Technology-NTNU, Trondheim, Norway

[8]School of Mechanical Engineering and Birck Nanotechnology Center, Purdue University, West Lafayette, Indiana 47907, USA

[9]Elmore Family School of Electrical and Computer Engineering, Birck Nanotechnology Center and Purdue Quantum Science and Engineering Institute, Purdue University, West Lafayette, IN, 47907 USA

[10]Department of Chemical and Biological Engineering, Illinois Institute of Technology, Chicago, IL, USA

*banasori@purdue.edu

Abstract

Two-dimensional transition metal carbides, nitrides, and carbonitrides, known as MXenes, hold potential in electrocatalytic applications. Tungsten (W) based-MXenes are of particular interest as they are predicted to have low overpotentials in hydrogen evolution reaction (HER). However, incorporating W into the MXene structure has proven difficult due to the calculated instability of its hypothetical MAX precursors. In this study, we present a theory-guided synthesis of a W-containing MXene, $W_2TiC_2T_x$, derived from a non-MAX nanolaminated ternary carbide $(W,Ti)_4C_{4-y}$ precursor by selective etching of one of the covalently bonded tungsten layers. Our results indicate the importance of W and Ti ordering and the presence of vacancy defects for the successful selective etching of the precursor. We confirm the atomistic out-of-plane ordering of W and Ti using density functional theory, Rietveld refinement, and electron microscopy methods. Additionally, the W-rich basal plane endows $W_2TiC_2T_x$ MXene with a remarkable HER overpotential (~144 mV at 10 mA/cm^2). This study adds a tungsten-containing MXene made from a covalently bonded non-MAX phase opening more ways to synthesize novel 2D materials.

Keywords:

MXenes, carbides, electrocatalyst, hydrogen evolution, electrocatalysis, 2D materials

Introduction

With the increasing visibility of climate change impacts attributed to fossil fuel consumption, there is a rising need for sustainable energy alternatives [1]. The key to a sustainable energy future lies in developing materials that can be used to generate and store energy. A crucial aspect of this pertains to the progress of eco-friendly hydrogen fuel cells and the production of hydrogen fuel via water electrolysis [2, 3, 4]. This paradigm shift necessitates the engineering of a proficient catalyst for the hydrogen evolution reaction (HER). Nevertheless, the sustainability of HER is hindered by the high cost of the most efficient noble metal catalysts, including platinum (Pt), iridium (Ir), and ruthenium (Ru) [5, 6]. Therefore, to design cost-effective HER catalysts, it is imperative to focus on developing new catalysts that possess the attributes of being scalable, effective, and reliable.

Tungsten (W) is relatively abundant in the earth's crust, with an abundance of approximately 1.3 parts per million (ppm) by weight compared to platinum's 0.005 ppm and iridium's 0.001 ppm [7, 8]. The high HER catalytic activity of tungsten-based materials (such as tungsten carbide, tungsten nitride, and tungsten oxide) can be attributed to their ability to bind hydrogen atoms [9, 10, 11, 12]. Tungsten has a relatively high electronegativity (2.36) and a low work function (4.8 eV), which allows it to easily accept electrons from hydrogen molecules and form strong tungsten-hydrogen bonds [13, 14, 15, 16]. Additionally, the electronic structure of tungsten-based materials can be tuned by controlling their composition and morphology, which can further enhance their HER activity [17, 18]. These features, in combination with their durability and resistance to corrosion under harsh operating conditions, make tungsten-based materials a promising alternative for HER compared to precious metal catalysts [19]. In recent years, layered W-based chalcogenides (WS_2, WSe_2, and WTe_2) have been progressively applied in the field of HER electrocatalysis due to their electronic properties and crystal structures [20, 21, 22, 23]. As a result, these W-based materials have opened exciting possibilities for affordable alternatives in catalytic and sustainable energy technologies [20, 21, 22, 23].

The growing palette of two-dimensional (2D) transition metal carbides, nitride, and carbonitrides, known as MXenes, are a promising class of electrocatalytic materials for clean energy applications [24, 25] because their 2D basal planes are electrochemically active [26], combined with their tunable chemistry [27, 28, 29, 30], electrical conductivity (up to 24,000 S/cm for $Ti_3C_2T_x$) [31], high mechanical strength (up to 386 GPa for $Nb_4C_3T_x$) [32], and thermal stability in inert environments [33, 34, 35].

MXenes have the chemical formula of $M_{n+1}X_nT_x$ (n = 1-4), where M stands for $n+1$ layers of one or more transition metals (usually from groups 4-6 of the periodic table), X stands for n layers of carbon or nitrogen which interleave the M layers, and T_x represents a variety of surface functional groups (commonly -O, -OH, -F) [36, 37, 38, 39]. MXenes are usually derived from their parent MAX phases, which are denoted by $M_{n+1}AX_n$, with A being an A-group element, usually groups 13-16 [28, 40]. The current synthesis approach of the majority of realized MXenes is through the selective etching of the A-group layers from their precursor MAX phase via different etching routes, including using hydrofluoric acid (HF) [41], HF-containing etchants with hydrochloric acid (HCl) [42], HF-forming etchants with fluoride salts (LiF, NH_4HF_2, FeF_3, KF, and NaF) and HCl [43, 44], molten salt etching (LiF, NaF, KF) [45], alkali-assisted hydrothermal etching [46], and electrochemical etching [47]. The use of top-down synthesis methods means processes to yield MXenes are scalable (up to 1 kg shown) [48, 49] which makes MXene a strong competitive 2D material for industrial-scale use.

MXenes' entire basal planes are catalytically active for HER, unlike 2D transition metal dichalcogenides, where only the 2D edges are catalytically active in most cases [26, 50, 51, 52, 53]. Thus, the basal plane provides more active sites in MXenes for HER. To date, Mo_2CT_x has shown the best HER performance among all MXenes with the lowest overpotential of 189 mV at 10 mA/cm^2 [26]. Beyond Mo_2CT_x, tungsten-based MXenes have garnered significant interest as they are anticipated to possess near-zero overpotentials with hydrogen adsorption-free energy ΔG_{ad}, approaching thermoneutral ($\Delta G_{ad} \rightarrow 0$), which makes them promising earth-abundant electrocatalysts for HER [51, 54]. However, as most MXenes are derived from their precursor MAX phases [55], incorporating W into MXene has proven difficult due to the calculated instability of its hypothetical precursor MAX phases, such as W_2AC and W_3AC_2 [51, 56]. To date, the only W-containing MAX phases are in-plane-ordered MAX (*i*-MAX) of $(W_{2/3}Sc_{1/3})_2AlC$ and $(W_{2/3}Y_{1/3})_2AlC$. Wet-chemical selective etching of these MAX phases using HF led to the removal of the Al layer along with scandium (Sc) or yttrium (Y). The resulting MXene exhibited ordered divacancies in which ~ 33% of the tungsten sites were vacant on each basal plane resulting in a $W_{1.33}CT_x$ MXene stoichiometry rather than the prototypical M_2CT_x. The measured HER overpotential of $W_{1.33}CT_x$ MXene was 320 mV at 10 mA/cm^2 [51]. Ordered divacancies provide metastable adsorption sites for hydrogen that require extended exposure time or repeated cycling to improve the reaction kinetics and HER electrocatalytic properties of $W_{1.33}CT_x$ MXene [57]. As a

result, there is a need for W-based MXenes in the form of M_2CT_x and $M_3C_2T_x$ with a minimum number of M vacancies on the MXene surfaces to maximize HER performance.

Based on theoretical predictions, W-containing MAX phases are inherently unstable in nature. However, the combination of W with other transition metals (for example, W with Ti) on the M sites has been predicted to form stable double-metal M_3AlC_2 and M_4AlC_3 MAX phases [58, 59]. Despite this prediction, many attempts, including several from our group, have resulted in no confirmed synthesis of W-containing M_3AlC_2 and M_4AlC_3 to date. Nevertheless, in 2019, a nano-laminated non-MAX ternary carbide $(W,Ti)_4C_{4-y}$ was synthesized in an attempt to make a hypothetical out-of-plane ordered W_2TiAlC_2 MAX phase [60]. In that work, a hexagonal and layered $(W,Ti)_4C_{4-y}$ was synthesized by pressureless sintering of elemental powder mixtures of W, Ti, Al, C in the molar ratio 2:1:1.1:2, which showed a hexagonal structure ($P6_3/mmc$) with twin plane layers of pure W and layers of mixed W and Ti all interwoven with layers of C as M_6C octahedra [60]. Even though aluminum is not present in the final crystal structure of $(W,Ti)_4C_{4-y}$, the presence of aluminum is crucial for the formation of this nanolaminated phase [60]. Further attempts were made to synthesize a W-containing MXene from this material, however, all the attempts until this current study have been unsuccessful [60].

In this study, we present the synthesis of $W_2TiC_2T_x$, the first W-containing, double-transition-metal (DTM) MXene, which is also among few MXenes that have been derived from a non-MAX precursor. Additionally, we synthesized this phase by etching covalently bonded layers of a transition metal from its layered carbide precursor. To do so, we modified the $(W,Ti)_4C_{4-y}$ phase using an excess amount of aluminum in the synthesis of the $(W,Ti)_4C_{4-y}$ precursor to improve the precursor quality [42, 61], which enabled the successful synthesis of $W_2TiC_2T_x$ MXene. The precursor and $W_2TiC_2T_x$ MXene were characterized in detail for their structure and morphology. We also measured the electrical conductivity as well as the linear and nonlinear optical properties of this new MXene for potential lasing and optoelectronic applications [62, 63]. Lastly, we studied the HER reaction kinetics of the $W_2TiC_2T_x$ MXene via first-principle density functional theory (DFT) calculations and measured electrocatalytic performance. Our results demonstrate that $W_2TiC_2T_x$ MXene exhibits highly efficient HER catalytic activity.

Results and Discussion

As discussed in the introduction, the only available precursor to make a tungsten M_3C_2 MXene is the non-MAX nanolaminated ternary carbide $(W,Ti)_4C_{4-y}$. This phase does not have any A-group layers and the corresponding metallic M-A layers, and there have been no known successful attempts for selective etching to remove atomic layers of W or Ti to form 2D carbide flakes of MXenes [60]. To investigate whether selective etching of any atomic layer (W- or Ti-layers) is possible, we first focused on computational methods using DFT to identify which atomic layer is most energetically favorable to be removed to yield a 2D carbide MXene, similar to the A-group layer removal in MAX to MXene synthesis. The $(W,Ti)_4C_{4-y}$ precursor was reported [60] to consist of one pure W layer with ~ 25 at% vacancies (shown as M1 in **Figure 1a**), two W-rich layers (labeled as M2) on either side of the M1 layer, and a Ti-rich layer (M3) in between the M2 layers (**Figure 1a**). We first modeled a "perfect" $(W,Ti)_4C_{4-y}$ structure with no W-Ti intermixing and no vacancies (M1 = 100 at% W, M2 = 100 at% W, M3 = 100 at% Ti). According to equations 1 and 2 in the Methods section, and as shown in **Figure S1a**, we identified that the formation energies toward removal of any layer are endothermic, with Ti M3 layer removal at +9.09 eV/Ti and removal of the W M1 layer being +3.21 eV/W. This suggested a preference for selective removal of the W M1 layer from the precursor, which could yield an idealized ordered double transition metal (DTM) MXene $W_2TiC_2T_x$ structure.

To investigate the effect of transition metal occupancy intermixing and the role of defects on the synthesizability of this potential 2D carbide $W_2TiC_2T_x$, we next considered intermixing between Ti and W in M2 and M3 layers in our DFT models to match the previously reported $(W,Ti)_4C_{4-y}$ phase composition [60]. Although our results for the reported structure with intermixing were still endothermic, they showed lower formation energies at +5.74 eV/Ti and +2.63 eV/W (**Figure S1b**). Next, we simulated a structure with 25 at% W vacancies in the W M1 layer in both non-intermixed and intermixed structures. The inclusion of 25 at% W vacancies resulted in negative formation energies at -3.75 eV/W and -4.81 eV/W for the non-intermixed and intermixed structures, respectively (**Figure S1c**). As a result, our DFT calculations suggest the presence of vacancies in the W M1 layer and intermixing of W and Ti in the M2 and M3 layers makes the selective etching of the W M1 layer to yield a W_2TiC_2-like structure more energetically favorable (**Figure 1b**).

Following the DFT prediction of the possibility of selective etching of the W-layers from $(W,Ti)_4C_{4-y}$ to make MXene, we prepared $(W,Ti)_4C_{4-y}$ precursor samples by mixing W:Ti:C in

2:1:2 molar ratio with 1.1 moles of Al [60] and sintering the mixed elemental powders at 1600 °C for 4 h under flowing argon (**Figure 1c**) (see Methods section). The X-ray diffraction (XRD) pattern of the synthesized precursor is shown in **Figure 1d**, which shows $(W,Ti)_4C_{4-y}$ as the main phase, and impurities such as Al_4W and $TiAl_3$ in agreement with the previous study [60]. Because we used 1.1 mol Al in the synthesis and the main $(W,Ti)_4C_{4-y}$ phase itself does not contain Al, we denoted this phase as $1.1Al–(W,Ti)_4C_{4-y}$. After preparing the precursor $1.1Al–(W,Ti)_4C_{4-y}$ powder, we then add the powder in 28.4 M HF for 96 h at 55 °C, a similar etching condition for the synthesis of a Mo-containing $M_3C_2T_x$ MXene [64]. After etching (see Methods), we compared the XRD patterns of as-synthesized and HF-etched $1.1Al–(W,Ti)_4C_{4-y}$ samples (**Figure 1d)** to identify any evidence of MXene formation. The first indication of 2D MXene formation from a precursor with 3D crystalline structure is usually the broadening and shift to lower 2θ of the (002) peak [28]. However, the XRD pattern after HF treatment shows $(W,Ti)_4C_{4-y}$ remained unchanged with no discernable broad peaks lower than the precursor (002) peak at $\sim 9.1°$ 2θ. The only change in the XRD patterns in **Figure 1d** is the disappearance of some peaks after HF treatment attributable to the dissolution of Al_4W and $TiAl_3$, in agreement with the first report on $(W,Ti)_4C_{4-y}$, where no MXene was reported [60].

Recently, it was shown that the inclusion of excess content of Al beyond the stoichiometric one mole during the reactive sintering of Ti_3AlC_2 MAX phase resulted in larger grain sizes and fewer defects (fewer metal vacancies and oxygen in the carbon sublattice) than those of the typically stoichiometrically prepared Ti_3AlC_2 [42, 60, 65]. While the excess Al (~ 2 moles instead of the required one mole) did not go to the structure, it was reported that its presence enhanced the quality of the resulting Ti_3AlC_2 MAX phase [65]. Overall, these studies suggested that the presence of ~ 2 moles of Al during the MAX sintering, while not going into the MAX structure, controls the stoichiometry and oxygen substitution in the carbon sublattice of the resulting MAX phase.

In this work, we used this strategy as inspiration in our approach to synthesize a modified $(W,Ti)_4C_{4-y}$ precursor for a successful synthesis of a W-containing MXene. We used two moles of Al (instead of 1.1 moles) and kept everything else unchanged. In other words, we mixed W:Ti:C with the molar ratio of 2:1:2 (the same as before) with two moles of Al (labeled as $2Al–(W,Ti)_4C_{4-y}$) and sintered the elemental mixture at the same conditions as $1.1Al–(W,Ti)_4C_{4-y}$ (see Methods section). The XRD pattern of the $2Al–(W,Ti)_4C_{4-y}$ powder after the 1600 ºC – 4 h showed similar

peaks as the 1.1Al–$(W,Ti)_4C_{4-y}$ indicating the majority phase is $(W,Ti)_4C_{4-y}$ with some intermetallic impurities (**Figure 1e**). We next added the 2Al–$(W,Ti)_4C_{4-y}$ in 28.4 M HF for 96 h at 55 °C with similar etching conditions as earlier. Similar to the HF-treated 1.1Al–$(W,Ti)_4C_{4-y}$ we observed the removal of Al_4W and $TiAl_3$ impurities. However, unlike the results of the 1.1Al–$(W,Ti)_4C_{4-y}$, we observed a new broad peak at ~ 7° 2θ (**Figure 1e** bottom pattern).

Figure 1: Density functional theory (DFT) and experimental approach for the synthesis of modified $(W,Ti)_4C_{4-y}$ precursor and its HF-etchability. A) Crystal structure of $(W,Ti)_4C_{4-y}$ precursor showing one pure M1 W layer with ~ 25 % vacancies, two M2 W-rich layers on either side of the M1 layer, and a M3 Ti-rich layer in between the M2 layers, b) Density functional theory (DFT) analysis of the synthesizability of $W_2TiC_2T_x$ MXene structure with intermixing between Ti and W without and with 25 at% W vacancies, c) Schematic of synthesis procedure for 1.1Al-$(W,Ti)_4C_{4-y}$ and 2Al-$(W,Ti)_4C_{4-y}$, d) XRD of as-synthesized and HF-etched 1.1Al-$(W,Ti)_4C_{4-y}$ e) XRD of as-synthesized and HF-etched 2Al-$(W,Ti)_4C_{4-y}$. f) Density functional theory (DFT) analysis of the synthesizability of a $W_2TiC_2T_x$ MXene structure out of the zAl-$(W,Ti)_4C_{4-y}$ precursor for z = 1.1, 2 based on Rietveld occupancies.

The appearance of the new low-angle broad peak at ~ 7° 2θ after selective etching resembled lower angle (002) peaks of other MXenes, such as $Ti_3C_2T_x$ at ~ 6-7° 2θ as compared to its precursor ~ 9.5° 2θ (002) peak of Ti_3AlC_2 MAX [35]. If we assume this peak was a shifted (002) peak from the

(W,Ti)$_4$C$_{4-y}$ precursor, the new etched phase has a c-lattice parameter (c-LP) of 27.77 Å, which is 8.89 Å larger than the c-LP of the (W,Ti)$_4$C$_{4-y}$ phase, consistent with changes in c-LP of Ti$_3$C$_2$T$_x$ from Ti$_3$AlC$_2$ [66, 67]. As a result, we speculated that the use of excess aluminum in the synthesis of the (W,Ti)$_4$C$_{4-y}$ precursor may have affected the structural occupancies favorable for selective etching to yield a 2D carbide from the nanolamellar (W,Ti)$_4$C$_{4-y}$ phase.

To investigate the difference in our as-synthesized 1.1Al–(W,Ti)$_4$C$_{4-y}$ and 2Al–(W,Ti)$_4$C$_{4-y}$ precursors, we analyzed the XRD results using Rietveld refinement methods to reveal any global scale (non-localized) changes in transition metal occupancies on the (W,Ti)$_4$C$_{4-y}$ precursor phase based on changing Al content in the powder mixture during the reactive sintering. As XRD methods are not accurate in analyzing carbon or oxygen occupancies, we focused this analysis on the transition metal occupancies in the various layers. To communicate the changes in occupancies on the transition metal "layers" within the nanolamellar (W,Ti)$_4$C$_{4-y}$ precursor, we labeled "M1", "M2", and "M3" in the (W,Ti)$_4$C$_{4-y}$ precursor the same way as described in **Figure 1a**, which correspond to the atomic sites (1/3, 2/3, 3/4), (1/3, 2/3, 0.1277), and (0, 0, 0), respectively. Comparing the occupancy of the transition metals in each site revealed that the use of two moles of Al in 2Al-(W,Ti)$_4$C$_{4-y}$ precursor has changed W (Ti) occupancy in the M1 site at +3 at% (0 at%), M2 site at +10 at% (+1 at%), and M3 site at +9 at% (-14 at%), compared to those of 1.1Al– (W,Ti)$_4$C$_{4-y}$. These changes indicate that more W appears to be in 2Al-(W,Ti)$_4$C$_{4-y}$ precursor as compared to the 1.1Al-(W,Ti)$_4$C$_{4-y}$, which might play a role in the formation and stability of a MXene from this structure. Using our Rietveld analysis ($\chi^2 < 0.1$), we noted that the M1 layer was solely occupied by W layers with vacancies, which our DFT calculations indicated as the most favorable atomic layer for selective etching to form a 2D structure.

The Rietveld results indicated substantial transition metal vacancies (~ 60 at%) in the W M1 layer in the synthesized (W,Ti)$_4$C$_{4-y}$ precursor phases (**Figure S2**). To best compare the occupancies as derived by Rietveld, we modeled a system with the same W-Ti intermixing and occupancies in different layers as our experimental samples (**Figure 1f**). Our DFT calculations showed that a (W,Ti)$_4$C$_{4-y}$ with occupancies similar to the synthesized 2Al–(W,Ti)$_4$C$_{4-y}$ requires lower energy (-3.06 eV/W) for removal of the W M1 layers compared to the structure with the occupancies of the 1.1Al–(W,Ti)$_4$C$_{4-y}$ (-2.33 eV/W). The lower predicted energy for the selective etching of the tungsten M1 layers in 2Al-(W,Ti)$_4$C$_{4-y}$ agrees with the successful experimental selective etching

in **Figure 1e**, where only the HF-treated 2Al-$(W,Ti)_4C_{4-y}$ demonstrated a clear, broad peak at ~ 7° 2θ. These findings suggest the slight change in transition metal occupancies in the $(W,Ti)_4C_{4-y}$ structure using two moles of Al in the starting powder forms a structure with an improved thermodynamic preference for selective removal of the W M1 layer to yield a 2D $W_2TiC_2T_x$ carbide structure. We note that our DFT results show that our 2Al-$(W,Ti)_4C_{4-y}$ is less favorable than the hypothetical $(W,Ti)_4C_{4-y}$ with intermixing and 25 at% W vacancies in the M1 layer (Figure 1b bottom panel), which suggests more control of transition metal occupancies and vacancies can further enhance the etching results, which requires further study. Additionally, this analysis does not take into consideration the effect of oxygen substitution in the carbon sublattice similar to previous reports on MAX phases [68], which may further have played a role in the transition metal occupancies and vacancies in the $(W,Ti)_4C_{4-y}$ structure and its subsequent potential for selective etching. However, for this first report of this potential MXene phase, we focused on 2Al-$(W,Ti)_4C_{4-y}$ that led to successful MXene formation.

To further validate the selective removal of the W layers, the byproducts formed after HF treatment of 2Al-$(W,Ti)_4C_{4-y}$ were studied. Our XRD and energy dispersive x-ray spectroscopy (EDS) in scanning electron microscope (SEM) (**Figure S3**) showed WO_3 in the supernatant after the first wash of the HF etching treatment. The presence of WO_3 suggests that W layers are being etched and WF_6 is formed, which then is transformed to WO_3 due to hydrolysis [69, 70] (Supplementary Information). Additionally, we analyzed the remaining non-etched precursor powder after the HF treatment and conducted Rietveld to identify any differences in W occupancy in the remaining non-etched $(W,Ti)_4C_{4-y}$ phase **(Figure S4)** compared with the original powder (**Figure S2**) to confirm the importance of W occupancy for etchability of the precursor. While the 1.1Al-$(W,Ti)_4C_{4-y}$ phase shows small changes in occupancy in layers layers post-HF treatment (within 3 at% of either W or Ti), the W M1 layers of the remaining non-etched 2Al-$(W,Ti)_4C_{4-y}$ powder post-HF-treated had ~ 10 at% increase of W as compared to the pre-HF treatment. Because these Rietveld refinements are on the remaining non-etched $(W,Ti)_4C_{4-y}$ precursor powder after the HF treatment, we believe they present the crystal structure and stoichiometry of the precursor powder which is not etchable. The increased W content in the M1 layer of the non-etched portion of our 2Al-$(W,Ti)_4C_{4-y}$ precursor again demonstrates that slight changes in W vacancy content in the M1 layers affect the etchability of the powder.

To further evaluate the effect of W vacancies, we conducted DFT calculations with different vacancy concentrations. $(W,Ti)_4C_{4-y}$ with stoichiometric M1 layer (no vacancy) results in an etching energy of +2.44 eV/W; however, when the W vacancy concentration increases in the M1 layer, the etching reaction becomes gradually more thermodynamically favorable (**Figure S5**) with etching energy of -1.15 and -2.33 eV/W for 22 % and 60 % W vacancy in the M1 layer, respectively. These results provide supportive evidence that W vacancies can promote the etching capability.

After determining the potential reaction mechanism to form a $W_2TiC_2T_x$ MXene structure from the 2Al-$(W,Ti)_4C_{4-y}$ precursor phase (**Figure 2a**), we next focused on morphological and structural characterization of the precursor, etched powder, and delaminated flakes (**Figure 2**) using SEM and XRD. **Figure 2b and c** show the 2Al-$(W,Ti)_4C_{4-y}$ grains that have layered morphology and plate-like clustered structures, and its XRD pattern with $(W,Ti)_4C_{4-y}$ as the majority phase. **Figure 2d** highlights the effect of HF on the precursor's morphology which causes the plate-like clusters of the 2Al-$(W,Ti)_4C_{4-y}$ powder (**Figure 2b**) to disassemble into nanoplate-like structures. While the XRD of the powder after HF treatment (**figure 2e**) still has the precursor peaks, new broad peaks appear at ~ 7, 14, 21, and 28° 2θ which suggest the formation of the (00L) peaks of MXenes [71].
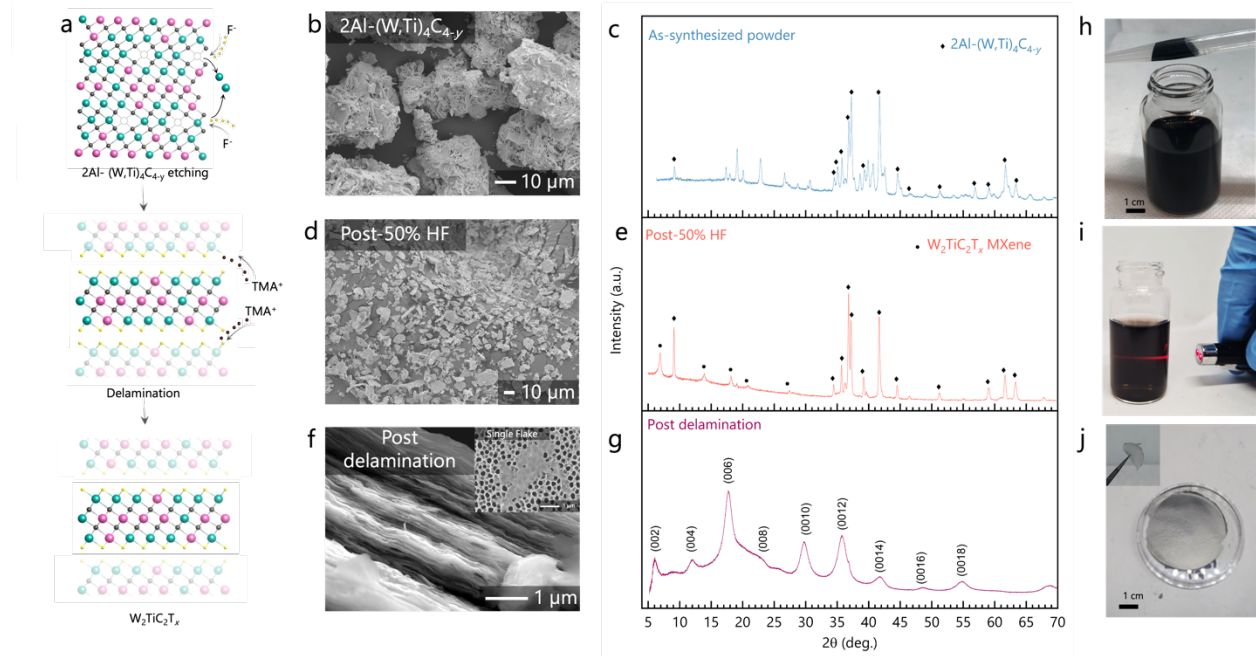

Figure 2. Step-by-step characterization of the 2Al-$(W_2Ti)_4C_{4-y}$ precursor to $W_2TiC_2T_x$ MXene synthesis process. A) Generalized etching and delamination reaction pathway. B) SEM and c) XRD of Al-$(W_2Ti)_4C_{4-y}$. d) SEM and e) XRD of HF etched $W_2TiC_2T_x$

MXene. F) SEM and g) XRD of free-standing $W_2TiC_2T_x$ MXene film (inset: single-to-few layer flake). H) Solution processable colloidal suspension of the delaminated $W_2TiC_2T_x$ MXene-like colloidal solution. I) Tyndall effect showing colloidal stability. J) Free-standing film prepared from the $W_2TiC_2T_x$ MXene-like colloidal solution and its flexible nature (inset).

After etching $2Al-(W,Ti)_4C_{4-y}$ for 96 h, the wet powders were then mixed in 6 wt% TMAOH at 55 °C for 4 h for TMA$^+$ intercalation [72] followed by repeated centrifugation and subsequent vortex mixing for delamination. The resulting dispersed black solution was then processed by final centrifugation at 2380 RCF for 30 minutes to separate single-to-few layer 2D flakes. **Figure 2f** displays the cross-sectional SEM of a free-standing film prepared by the vacuum filtration of the colloidal solution. This cross-section image shows the stacking of many 2D flakes and an electron-translucent single flake is shown in the **Figure 2f inset**. The XRD pattern of the free-standing film shows only broad (00L) peaks reminiscent of MXene [71] (**Figure 2g**). Visually, the aqueous solution color was dark grey and solution processible (**Figure 2h**) and a Tyndall effect was observed (**Figure 2i**) in a dilute solution which is attributed to the formation of stable aqueous dispersions. The as-fabricated, additive-free, free-standing film (**Figure 2j**) was brittle in nature with metallic luster and did not require any post-treatment.

To further confirm the selective etching of the pure tungsten layers and the formation of 2D MXene layers, we conducted scanning transmission electron microscopy (STEM) in the high-angle annular dark-field condition (HAADF). The cross-sectional atomic resolution images of the MXene layers acquired via aberration-corrected STEM show that the horizontally aligned 2D layers are made of three-atom-thick layers (**Figure 3a**). To further understand the arrangement and ordering of the atoms, we looked at individual layers at higher magnifications (**Figure 3b**), which showed that the atoms in the outer layers had higher brightness than the atoms in the inner layer. These STEM results confirmed that three-atom-thick layers are formed where the outer atoms are heavier than the middle atoms, which appears analogous to an ordered 2D double-metal M_3C_2 MXene with W-rich outer M layers and Ti-rich inner M layer. These results agree with our DFT predictions (**Figures 1f**) that pure W layers are etched from the $(W,Ti)_4C_{4-y}$ precursor structure and results in $W_2TiC_2T_x$ MXene. The plan-view STEM micrographs of $W_2TiC_2T_x$ flakes (**Figure S6**) further show the planar view of the 2D MXene sheets. The atomic resolution STEM micrographs include the EDX spectra and line scans which confirm the presence of W and Ti ordering in the layered structure (**Figure S7**).
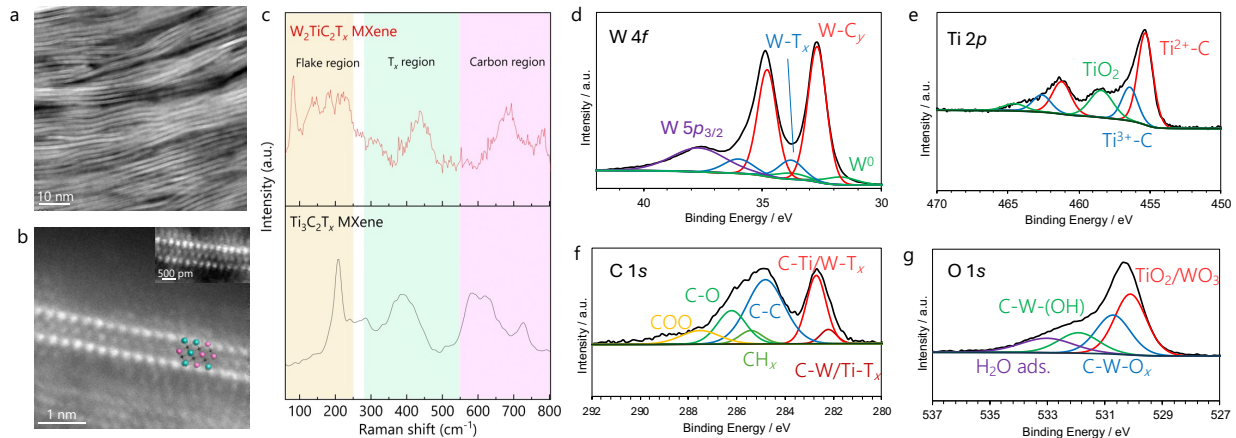
Figure 3. (a) Cross-sectional HAADF-STEM image of $W_2TiC_2T_x$ MXene layers in the horizontally aligned MXene pattern prepared by focused ion beam (FIB) lift out, and (b) atomic resolution HAADF-STEM image of $W_2TiC_2T_x$ MXene layers. STEM images show that the horizontally aligned MXene patterns have well-stacked layers of W and Ti. The light elements of the surface termination groups (O, H, and F) cannot be seen between the layers, but the larger and non-uniform spacing seen in Figure 4b indicates the weak interactions between the MXene layers after etching and the formation of a 2D structure. (c) Raman spectra of $W_2TiC_2T_x$ MXene compared with $Ti_3C_2T_x$ MXene. (d-f) XPS of $W_2TiC_2T_x$ MXene film for W4f (d), Ti2p (e), C1s (f), and O1s (g).

After investigating the cross-section of the free-standing films and single-to-few layered flakes analogous to a M_3C_2 MXene structure, we measured the Raman spectrum of $W_2TiC_2T_x$ MXene film and compared it with the well-studied $Ti_3C_2T_x$ MXene **(Figure 3c),** which has an identical $M_3C_2T_x$ structure. The spectral positions were determined by fitting the average Raman response of $W_2TiC_2T_x$ and $Ti_3C_2T_x$ MXene to a sum of Lorentzian peak shapes consistent in methodology to the previous reports (**Figure S8**) [73]. We observed similarities in the average Raman spectra for both the MXenes having a characteristic response that is consistent with a "pseudo" $P6_3/mmc$ space group [73, 74]. For example, $W_2TiC_2T_x$ MXene exhibits the expected spectral responses in three distinct energy regions termed as, flake (50-270 cm^{-1}), T_x (230-500 cm^{-1}), and carbon (470-800 cm^{-1}) bands corresponding to vibrations of C-(W,Ti)-O, surface terminations, and carbon groups, respectively. The similarities in Raman response between the two structures and their consistency with previous reports further corroborate the conclusion from XRD and STEM on the $W_2TiC_2T_x$ MXene structure.

Moreover, based on our observations, analyzing the broadening and energy shifts in the $Ti_3C_2T_x$ and $W_2TiC_2T_x$ MXene compositions provides insight into how the W incorporates into the lattice structure, influencing the bonding and scattering. Notably, the broadening in $W_2TiC_2T_x$ MXene is larger in the flake and carbon spectral regions, which probe the bonds with the W-Ti species

(**Figure 3c**). In contrast, the intermediate energy in the T_x region has a spectral width that is relatively unaffected. The addition of heavier W atoms disrupts the periodicity of the crystal lattice causing the movement of these atoms or the bonds attached to them. This results in shortened phonon lifetime, which is observed as a broadening of the Raman response in both the flake- and carbon spectral regions. In addition to broadening in the spectra, substantial and quantified peak shifts are indicative of bond strength alterations that occur with the addition of W. The phonon energies increase with lighter atoms and stronger bonds. Expectedly, the low energy flake spectral feature is indicative of a group vibration that red-shifts in $W_2TiC_2T_x$ MXene compared to $Ti_3C_2T_x$ MXene. This is attributable to the introduction of substantially heavier W. On the other hand, phonon energies for both the T_x and carbon regions blue-shift with the addition of heavier W suggesting a significant increase in bond strength for these vibrations. Quantitatively, the intensity in the carbon region is found to increase from 730 cm^{-1} to 774 cm^{-1} from the $Ti_3C_2T_x$ to the $W_2TiC_2T_x$ MXene, respectively, despite the increase in atomic mass (**Figure S8**). This large increase in energy indicates that the addition of heavier W in the $W_2TiC_2T_x$ MXene induces a substantial change in the bonding environment portending implications for the chemical, optical, and mechanical properties.

We next focused on X-ray photoelectron spectroscopy (XPS) of the $W_2TiC_2T_x$ free-standing film (**Figure 3d-g**) to further confirm that the material exhibits carbide (i.e., a 2D MXene) and not oxide-like (i.e., oxide nanorods or 2D oxides [75, 76]) coordination states. Full XPS spectra and deconvolutions of the precursor powders with the peak deconvolution tables are also shown in **Figures S9** and Table S1, respectively. We hypothesized that, if W-Ti oxide or carbo-oxide complexes are formed, this should be reflected in XPS patterns with clear and dominant TiO_x or WO_x patterns. However, for the W 4f and Ti 2p pattern (**Figure 3d and e**, respectively), the deconvoluted MO_x peaks were either lower in intensity or non-existent compared to the M-C peaks, which is different from oxides produced from carbide structures [77]. This XPS data does suggest that the transition metals bond in M-C or T_x-M-C states, which is consistent with the coordination states of transition metals within previously reported MXenes [78, 79]. Further analysis of the C 1s or O 1s spectra (**Figures 3f, g**, respectively) also shows consistent behavior with -O or -OH terminated MXenes [78, 79]. By analyzing these peaks and the F-content, we can roughly calculate the surface group content to be that of roughly 37 at%, 28 at%, and 35 at% O, (OH), and F, respectively, which shows a mixed surface termination $W_2TiC_2(O_{0.74}(OH)_{0.56}F_{0.70})$ MXene.

Therefore, based on the STEM, Raman, and XPS data shown in **Figure 3**, combined with the XRD and SEM data presented in Figures 1 and 2, we are confident that that the HF and TMAOH treatment of the 2Al-$(W,Ti)_4C_{4-y}$ precursor powder in-fact produced a $W_2TiC_2T_x$ 2D MXene.

After confirming the synthesis of a $W_2TiC_2T_x$ MXene from the non-MAX $(W,Ti)_4C_{4-y}$ phase, we next characterized the HER behavior of this $W_2TiC_2T_x$ MXene. We first employed DFT methods to study the surface interactions and electrocatalytic activity during HER. The intermixed surfaces of Ti and W were simulated to observe the adsorption behavior of H with varying terminations **(Figure 4a)**. Because of the existence of the WO peaks found in XPS (**Figure 3d**), in other words, undercoordinated surface W atoms, we considered surface termination vacancies in DFT to study their effects on H adsorption. Additionally, it is believed that, by interacting with an acidic environment and potential bias, the surface termination –O atoms are reduced to –OH groups [80, 81]. For this reason, only –OH and –F terminations, along with their corresponding vacancies, are considered for HER (**Figure 4a)** and their free energy diagram (FED) indicating the adsorption energies is shown in **Figure 4b**. Our calculations suggest H adsorption energies are -1.55 and -0.37 eV over the OH- and F-terminated surfaces, respectively. Over the OH-terminated surface, H is adsorbed atop the W atom, **Figure 4a**, while on the F-terminated surface, it forms a 3-fold site with two W and one Ti, **Figure 4a**. At the –OH and –F vacancy sites, H adsorption is also at the 3-fold site with two W and one Ti (**Figure 4a**), with adsorption energies of -0.57 and -0.71 eV, respectively. On the non-intermixed surface (pure W), the H adsorption is on top of W (**Figure S10a)** with binding energy of -1.79 eV and -3.71 eV on OH- and F-terminated surfaces (**Figure S10b**). However, when considering the –OH and –F vacancy sites, the preferred binding sites for H become the vacancy sites (3-fold site) with the same H adsorption energy of -0.63 eV (**Figure S10a, b**). By computing the overall DOS of OH- and F-terminated surfaces with and without Ti-W intermixing (**Figure S11)**, the DOS of the intermixed surfaces shifts to lower energy compared with the non-intermixed surfaces. The d-band center of the intermixed OH- and F-terminated surfaces are lower in energy (both at -2.17 eV) compared with the non-intermixed cases (-1.96 and -2.12 eV for –OH and –F terminations). According to the d-band center theory [82], a lower d-band center results in weaker binding energy, which explains the reason for weaker H adsorption on the intermixed surfaces. Additionally, the mixed OH- and F-terminated MXene surfaces are considered to investigate the HER activity (**Figure S12**). Over the non-intermixed surface, the H adsorption over the periodic surface is 0.16 eV; however, considering the –OH and –F vacancies,

the H adsorption becomes -0.84 and -1.06 eV, respectively (**Figure S12d**). On the intermixed surface, H adsorption over the periodic surface is -0.31 eV, and the adsorption over –OH and –F vacancies results in H adsorption energies of -0.67 and -0.77 eV (**Figure S12h**).
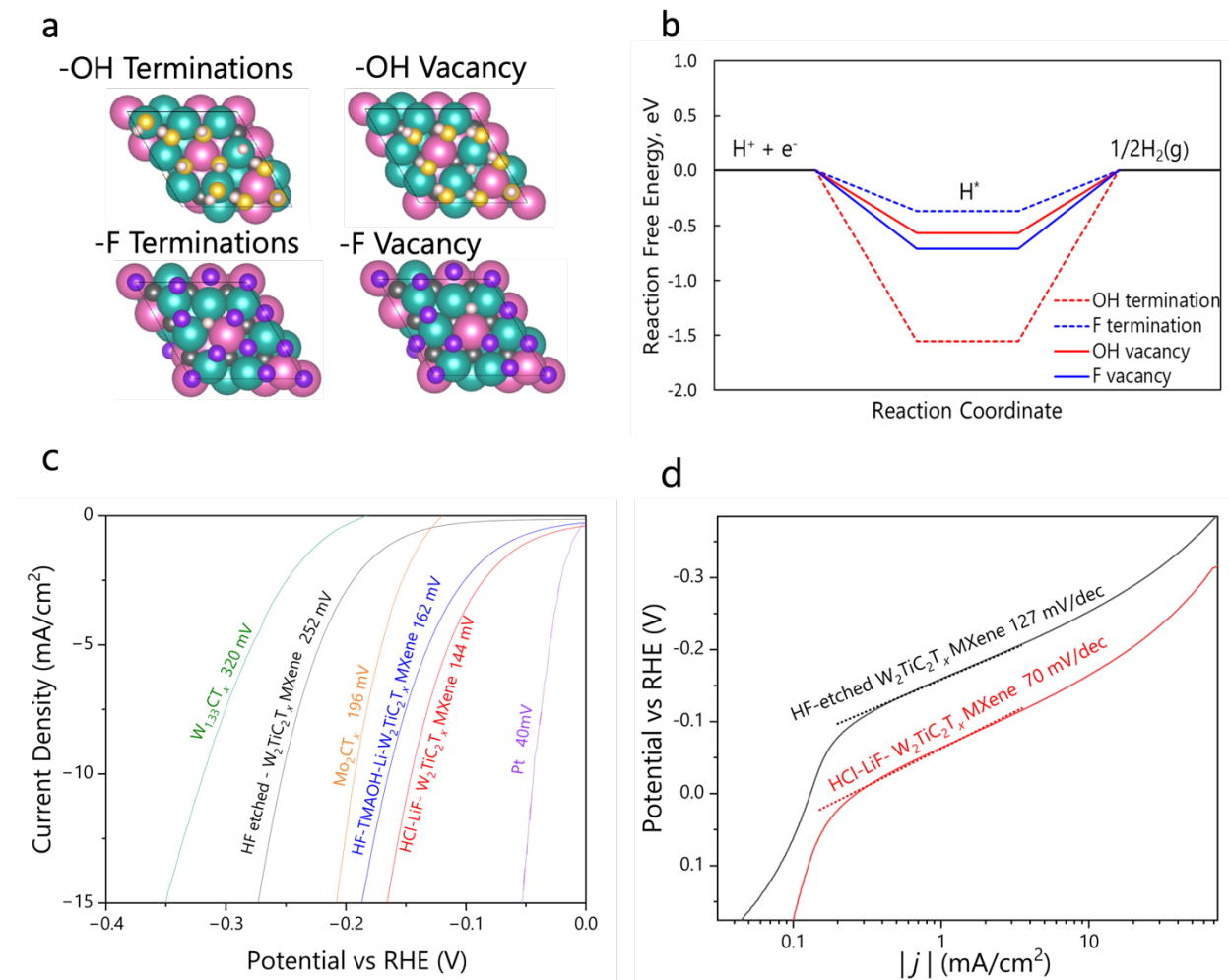

Figure 4. HER activity of $W_2TiC_2T_x$ MXenes: The HER activity of $W_2TiC_2T_x$ MXene has been performed by well-defined density functional theory calculations. (a) Optimized structures of the adsorption site of H^+ on intermixed Ti and W with all -OH terminations, -OH vacancy, -F terminations, and –F vacancy. (b) Free energy diagram of HER over MXene surface with Ti-W intermixing. The prepared MXenes electrode was examined in a three-electrode electrochemical cell using a rotating disk electrode apparatus at 1600 rpm in 0.5 M H_2SO_4. The results present (c) Linear sweep voltammetry (LSV) curves of studied $W_2TiC_2T_x$ MXenes. We compared the HER activity of HCl-LiF-$W_2TiC_2T_x$ MXene and HF-etched $W_2TiC_2T_x$ MXene. The LSV results show the lowest overpotential of 144 mV for HCl-LiF-$W_2TiC_2T_x$ MXenes. (d) Tafel analysis of studied $W_2TiC_2T_x$ MXenes for HER indicates a Tafel slope of 70 mV/dec. The HER activity of $W_2TiC_2T_x$ MXene may be linked to the highly active and ordered basal-plane vacancies of W.

Further, we experimentally studied the HER catalytic behavior of $W_2TiC_2T_x$ MXene. It has been observed that HF-TMAOH MXenes possess TMA^+ cations on their surfaces, which hinder their

adhesion to glassy carbon electrodes [83]. Consequently, we employed two distinct approaches to investigate the HER performance of $W_2TiC_2T_x$ MXene, (i) Li cation exchange and (ii) MILD HCl-LiF route used to synthesize $W_2TiC_2T_x$ MXene (**Figure S13**) as discussed in the Methods section. We first drop-cast $W_2TiC_2T_x$ MXene onto glassy carbon electrodes using Nafion 117 as a binder. The prepared $W_2TiC_2T_x$ MXene electrode was then examined in a three-electrode electrochemical cell using a rotating disk electrode apparatus at 1600 RPM in 0.5 M H_2SO_4. In the resultant linear sweep voltammograms (LSVs), we noted that $W_2TiC_2T_x$ MXene was found to be a more active catalyst toward electrochemical water reduction reaction (**Figure 4c)**. We compared the HER activity of HF-etched $W_2TiC_2T_x$ MXene multilayer powder, HF-TMAOH delaminated and Li-exchanged $W_2TiC_2T_x$ MXene (labeled as HF-TMAOH/Li-exchanged $W_2TiC_2T_x$) and HCl-LiF-$W_2TiC_2T_x$ MXene. The LSV results show an overpotential of 144 mV for HCl-LiF-$W_2TiC_2T_x$ MXene, which is about 1.55 times lower than that of HF-etched $W_2TiC_2T_x$ MXene (252 mV). Tafel slopes derived from the potential vs. current density plots (**Figure 4d**) illustrate that HCl-LiF-$W_2TiC_2T_x$ MXene continues to outperform as compared to other HF etched $W_2TiC_2T_x$ MXene with a slope of 70 mV/dec. This enhanced HER activity of $W_2TiC_2T_x$ MXene may be linked to the highly active and ordered basal-plane of W and the presence of vacancies.

We next compared the HER catalytic behavior of our $W_2TiC_2T_x$ MXene to other MXenes, such as $W_{1.33}CT_x$ MXenes and our lab synthesized Mo_2CT_x MXenes and found that HCl-LiF-$W_2TiC_2T_x$ MXene overpotential (144 mV) is about 1.12, 1.75, 1.97, 2.22, and 1.36 times lower than that of HF-TMAOH-Li-exchanged $W_2TiC_2T_x$ MXene (162 mV), etched $W_2TiC_2T_x$ MXene (252 mV), $W_{1.33}CT_x$ MXenes (320 mV), and Mo_2CT_x MXenes (196 mV), respectively [51, 52]. In comparison with other MXenes, we noted that $W_2TiC_2T_x$ MXene outperformed electrochemical HER as shown in **Figure 4c**, presenting a new and promising catalyst for HER with the highly HER active W-containing basal planes.

We next investigated the electronic and optoelectronic behavior of $W_2TiC_2T_x$ MXene. The resistivity *R* and conductivity *c* temperature dependance measurements **(Figure S14)** indicated R increasing with increasing temperature, with RT conductivity equal to 427 S/cm, which is comparable with the V_2C MXene (*c* =384.6 S/cm) [84]. The measured conductivity dependence of $W_2TiC_2T_x$ MXene film can be described by two models: thermally activated Arrhenius type and low-temperature variable-range-hopping (VRH) model. The data were fitted using these two

models, separately for the low and high-temperature parts. Low-temperature data of temperature dependence of conductivity are best described by the VRH model (**Figures S15**) with coeff. 1/2, which corresponds to one-dimensional conductivity or Coulombic effect [85, 86]. Low-temperature conductivity following the VRH model can be mostly explained by the inter-flake hopping due to the flake-like structure of thin films, as has been demonstrated for several MXenes [85]. The high-temperature response, however, follows an Arrhenius model best. Magnetoresistance of $W_2TiC_2T_x$ MXene film is positive at 1.8 K (**Figure S16**), which is typical for standard metals and semiconductors when the applied magnetic field in a direction perpendicular to the film causes drift of electrons, hence the increase of resistivity with increasing magnetic field.

Further, $W_2TiC_2T_x$ MXene also boasts a unique range of optical properties in comparison to other members of the MXene family. The absorption spectrum of ~ 150-nm-thick spin-coated $W_2TiC_2T_x$ film **(Figure S17)** indicates the material is highly absorptive in the ultraviolet spectra and is transmissive in the infrared. These characteristics are similar to that of $Mo_2TiC_2T_x$ and Mo_2CT_x MXenes [87]. Additionally, a distinct step-like pattern is seen on the blue side of the spectrum, indicating that the absorption is generated from multiple distinct transitions. While other MXenes (such as Mo_2CT_x, $Mo_2TiC_2T_x$, Nb_2CT_x, $Ti_3C_2T_x$, Ti_2CT_x, V_2CT_x) have local minimums or maximums in absorbance spectrum [87] and $W_2TiC_2T_x$ has a plateau in absorption that occurs near 400 nm. This could suggest the broadening of energy bands or more complex band interactions.

Next, we measured the nonlinear optical transmission of the $W_2TiC_2T_x$ MXene with the I-scan technique [88] using an 800 nm wavelength femtosecond pulsed laser, revealing reverse saturable absorption (RSA) behavior (i.e., increased input light intensity leads to a higher absorption) [89]. As shown in **Figure S18,** three distinct regions of varying slopes are evident. A common explanation for nonlinear dynamics in absorbing media is based on the absorption cross-sections of various energy levels. For a multi-level system, as is suggested for $W_2TiC_2T_x$ by the linear absorption spectra, plateaus, and other non-monatomic trends arise from changing equilibrium dynamics at different incident power [89]. This unique behavior is not commonly reported in MXene literature and warrants further investigation. More generally, these results suggest the use of $W_2TiC_2T_x$ for optical limiting applications or all-optical switching.

Conclusions

In summary, we have reported the theory-guided synthesis of W-containing MXene $W_2TiC_2T_x$, by selective etching of the covalently bonded W-layers from a modified nanolaminated ternary carbide $(W,Ti)_4C_{4-y}$ precursor, and characterized its structure and composition in-depth using a combination of XRD, XPS, TEM, EDS, Rietveld, and DFT methods. W-rich basal plane endows $W_2TiC_2T_x$ MXene with remarkable electrocatalytic HER performance in terms of lowest HER overpotential (~144 mV) under acidic conditions, which is supported by DFT studies. HER activity of $W_2TiC_2T_x$ MXene may be linked to W's highly active and ordered basal planes. To advance the design of HER catalysts for clean energy applications, it is crucial to increase efforts toward the continuous exploration of W-based MXenes, due to the significant potential for advancement presented by their catalytic behaviors and earth-abundance. Further, our studies on the electronic and optoelectronic behavior of $W_2TiC_2T_x$ suggest that this MXene could be used for optical limiting, all-optical switching, and other photonic and optoelectronic applications.

Material and Methods

(W,Ti)$_4$C$_{4-y}$ precursor synthesis

$(W,Ti)_4C_{4-y}$ precursor was synthesized using elemental powders of tungsten, titanium, aluminum, and calcined coke which were mixed in stoichiometric 2:1:1.1:2 and excess-metal 2:1:2:2 molar ratio. The powders were then jar-milled in 250 mL Nalgene high-density polyethylene bottles (~ 10 g batch) with yttria-stabilized zirconia balls for 18 h in 2:1 ball-to-powder mass ratio without any shear at 60 RPM. The precursor powder was not sieved after jar-milling and then packed into an alumina crucible. The top of the crucible was covered with graphite foil and placed in a high-temperature tube furnace (Carbolite Gero, 1700 °C model) for reactive pressureless sintering. Initially, the furnace was purged with argon (99.999 % purity) for 20 minutes at room temperature. After purging, the ball-milled precursor powders were heated to 1600 °C at a 3.5 °C/min ramp rate and held for 4 hours under a constant argon flow. After 4 hours, the furnace was cooled to room temperature at a 10 °C/min. Then the alumina crucible containing sintered billets of stoichiometric 1.1Al – $(W,Ti)_4C_{4-y}$ and excess-metal 2Al – $(W,Ti)_4C_{4-y}$ precursor were removed and drilled to a fine powder using a TiN coated drill bit in a drill press setup.

W$_2$TiC$_2$T$_x$ MXene synthesis

The synthesized precursor was sieved using a 40 μm sieve before MXene synthesis. For 1g of $(W,Ti)_4C_{4-y}$ precursor, 10 mL of 28.4 M HF etchant was used. The etchant was taken in a 60 mL Nalgene high-density polyethylene bottle with a magnetic stir bar. Then, the $(W,Ti)_4C_{4-y}$ presursor was added slowly at a rate of ~ 0.5 g/minute. The etching reaction was carried out at 55 °C for 96 hours in the hot plate at 400 RPM. The reaction vessel should be capped with a condenser column on the top to release evolved gases and entrap vapors during the reaction. The etched multilayered MXene powder was washed to neutral pH with ~ 250 mL deionized water by repeated

centrifugation in an Eppendorf centrifuge at 3234 RCF for 5 minutes. Then the neutralized solution was vacuum-filtered using a 0.8 µm filter membrane and the wet masses were recorded directly after. For delamination, tetramethylammonium hydroxide (TMAOH) solution (25 wt% stock, Fisher Scientific) with 10 mL of 6 % TMAOH per gram of etched $W_2TiC_2T_x$ MXene was used, and the reaction was carried out 55 °C for 4 h with continuous stirring at 400 RPM. TMA^+ intercalated $W_2TiC_2T_x$ MXene was washed with ~ 250 mL deionized water for every 1 g of the precursor by repeated centrifugation at 21913 RCF in the Thermo Scientific centrifuge for 5 minutes followed by decantation until neutral pH. Then the washed $W_2TiC_2T_x$ MXene clay was delaminated by mechanical agitation using vortex mixer for 30 minutes. $W_2TiC_2T_x$ MXene clay was re-suspended in deionized water and vortexed for 30 minutes to isolate single-to-few MXene layers. $W_2TiC_2T_x$ MXene colloidal suspension was then processed by final centrifugation at 2380 RCF for 30 minutes. The supernatant containing single-to-few layered $W_2TiC_2T_x$ MXene was collected, and vacuum filtered using 0.25 µm filter membrane to prepare MXene films.

For HER studies, two approaches were followed (i) cation exchange for HF-TMAOH delaminated $W_2TiC_2T_x$ MXene, and (ii) minimally intensive layer delamination (MILD) route using HCl-LiF for the synthesis of $W_2TiC_2T_x$ MXene. The experimental differences are described as follows: (i) cation exchange using 1:50x ratio of HF-TMAOH delaminated MXene to LiCl salt at room temperature for 1 h with 400 RPM stirring, and (ii) 12 M LiF and 9 M HCl mixture for 1 g $(W,Ti)_4C_{4-x}$ precursor at 55 °C for 96 h with continuous stirring at 400 RPM. The resulting powders were centrifuged at 21913 RCF in the Thermo Scientific centrifuge for 5 minutes followed by decantation until neutral pH.

Characterization techniques

X-ray diffraction (XRD) patterns of the as-synthesized $(W,Ti)_4C_{4-y}$ precursors and $W_2TiC_2T_x$ MXene were analyzed using a Bruker D8 X-ray diffractometer with a Cu Kα ($\lambda = 1.5406$ Å) emitter and a VANTEC 500 two-dimensional x-ray detector (XRD^2). A corundum standard was used to ensure each detector was calibrated. The precursor samples were mounted on Kapton tapes and scanned from 5 ° to 75 ° with a step size of 5 ° and a dwell time of 30 seconds per step. The $(W_2Ti)C_2T_x$ MXene films made from vacuum filtration were annealed in the vacuum at 200 °C for 18 hours to remove the water entrapped between the layers and then analyzed using XRD. The traditional XRD plots were obtained by merging and integrating the XRD^2 data in DIFFRAC.SUITE EVA software. For Rietveld refinement, the XRD patterns were recorded using a Lynxeye detector and scanned from 5 ° to 75 ° with a step size of 0.02 ° and dwell time of 1 second per step.

Scanning electron microscopy (SEM) was performed on a JEOL JSM-7800F at an acceleration voltage of 15 kV to study the flake size and surface morphology. The solution concentration was maintained at < 0.1 mg/mL and loaded on an anodic disc followed by vacuum drying for 2 hours. The samples were gold sputtered to reduce the charging. Energy dispersive X-ray spectroscopy (EDS) measurements were conducted using an EDAX Octane Silicon Drift Detector in point scan mode with a 30s exposure time. The EDS data was subsequently analyzed using EDAX TEAM software.

Cross-sectional lamella for scanning transmission electron microscopy characterization was prepared by conventional focused ion beam (FIB) lift-out on a Zeiss Nvision40. The thinning process was followed by low-energy final polishing in the FIB (2 kV and 60 pA) to minimize the

ion-induced damage and to obtain a foil with a uniform thickness. During the preparation process, the site of interest was covered with a protective layer through FIB-assisted carbon deposition.
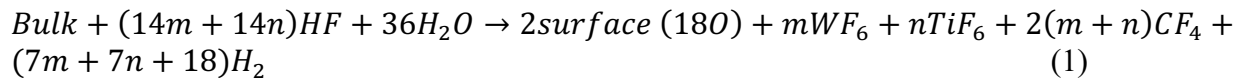
Scanning transmission electron microscope images were acquired in the high-angle annular dark-field (HAADF-STEM) condition on an aberration-corrected (double Cs-corrected) Thermo Fisher Scientific Titan-Themis 60-300 operated at 200 kV and using a beam current of 100 pA. This microscope is equipped with a high-brightness Schottky X-FEG, a Super-X EDS system comprising four silicon drift detectors, and Velox acquisition software. Energy dispersive X-ray spectroscopy (EDS) data were collected in the form of spectrum images, in which a focused electron probe was scanned in raster across a region of interest in the scanning TEM (STEM) mode.

X-ray photoelectron spectroscopy (XPS) spectra were collected for each sample on a Thermo K-Alpha XPS system with a spot size of 400 μm and a resolution of 0.1 eV. All spectra were processed using Thermo Avantage, which is a software package provided through ThermoScientific.

Computational Studies

Density functional theory (DFT) calculations were carried out using the Vienna ab initio Simulation Package (VASP) [90, 91]. The projector augmented (PAW) method was used to describe the wave function of the ionic cores; then the generalized gradients approximation (GGA) was used with Perdew-Burke-Ernzerhof (PBE) functional [92]. The cutoff energy for bulk and surface geometry optimization was 520 eV and 400 eV, respectively. The Monkhost-pack mesh [93] of $6 \times 6 \times 1$ and $3 \times 3 \times 1$ was used for bulk and surface geometry optimization, respectively. The break condition for ionic relaxation was set as 1E-6 eV. The geometry optimization was stopped when the forces on atoms were smaller than 0.02 eV/Å. To account for the dispersion forces, Grimme's DFT-D2 method [94] was employed, which has been proven sufficient for layered structures [95, 96, 97, 98]. The computed lattice for W containing MXene is a = b = 3.04 Å, and c = 20.22 Å which agrees well with reported values in the literature [60].

To study the surface chemistry and adsorption interaction between the reaction intermediates and the catalyst surface, periodic 3×3 surfaces that are passivated by 18 O atoms with and without intermixing between Ti and W were cleaved along the (001) direction from the optimized bulk structure. Furthermore, the reaction proposed by equation (4), where m and n represent numbers of Ti and W atoms in the etched layer, is used to mimic the selective etching process. Since the etching process takes place with HF, we assume the formed products are WF_6, TiF_4, CF_4, and H_2.

$$Bulk + (14m + 14n)HF + 36H_2O \rightarrow 2surface\ (18O) + mWF_6 + nTiF_6 + 2(m+n)CF_4 + (7m + 7n + 18)H_2 \tag{1}$$

The reaction energy, ΔE, for etching were then calculated using equation (2) based on reaction proposed by equation (1).

$$\Delta E = \frac{2*E_{surface(18O)} + m*E_{WF_6} + n*E_{TiF_4} + 2(m+n)E_{CF_4} + (7m+7n+18)E_{H_2} - E_{bulk} - (14m+14n)E_{HF} - 36E_{H_2O}}{m+n}$$
(2)

To obtain the reaction free energy, ΔG, the equation 2 was used [99]:

$$\Delta G = \Delta E + \Delta ZPE - T\Delta S \tag{3}$$

where ΔE represents the total energy change upon reaction, which can be directly obtained from DFT calculations. ΔZPE and $T\Delta S$ represent the changes in zero point-energy and entropic contribution, which can be calculated using statistical dynamics approximation using vibrational frequencies from DFT calculations as discussed in the literature [100].

For all the gas phase calculations, the molecules, i.e. H_2 and H_2O, were introduced into a box with dimension of $25 \times 25 \times 25$ Å for geometry optimization using single Γ k-point. Furthermore, the total energy of H, OH, and O was calculated using H_2 and H_2O as reference states [80, 81] as described by equation 1-3.

$$E_H = \frac{1}{2} E_{H_2} \tag{4}$$

$$E_{OH} = E_{H_2O} - \frac{1}{2} E_{H_2} \tag{5}$$

$$E_O = E_{H_2O} - E_{H_2} \tag{6}$$

Electrochemical HER studies

We drop-cast $W_2TiC_2T_x$ MXenes onto glassy carbon electrodes using Nafion as a binder. This process involved mixing 5 mg of $W_2TiC_2T_x$ MXene with a 5% solution of 20 µL Nafion 117 in the water and ethanol mixture, followed by the drop-casting of 20 µL of this mixture on the glassy carbon electrode. $W_2TiC_2T_x$ MXene was then examined in a three-electrode electrochemical cell using a rotating disk electrode apparatus (AUTOLAB, Metrohm) at 1600 RPM in 0.5 M H_2SO_4. The $W_2TiC_2T_x$ MXenes onto glassy carbon were used as the working electrode, Pt-sheet as the counter electrode and Ag/AgCl as a reference electrode. The electrochemical HER studies include linear sweep voltammetry (sweep rate of 1 mV/s).

Transport properties

Thin film of $W_2TiC_2T_x$ MXene was prepared by vacuum filtration of suspension containing delaminated single sheets. To remove the intercalated water between the stacked MXene flakes, the free-standing MXene films were annealed at 200 °C in vacuum. Subsequently, the sample was annealed at 500 °C in the vacuum which is known as the approach of removing the -OH functionalization, typically causing the drop of resistivity. The thickness of the film was estimated from SEM images ~ 5 µm. To measure transport properties, the sample was wired by four probe method, using copper wires and silver paint by TedPella, with distance between contacts app. 1.5 mm.

Temperature dependence of resistance of thin film (R(T)) in the temperature range of 1.8-300 K and magnetoresistance (magnetic field -9 - 9 T) at 1.8 K were measured using Quantum Design PPMS DynaCool system. Excitation current was 0.1 mA with a frequency 18.3 Hz. Data were collected in the temperature sweep mode from 300 down to 1.8 K. Conductivity was calculated using measured film thickness and distance between contacts. Data were fit by models of Variable Range Hopping and thermally activated Arrhenius conductivity, using custom-written Matlab script(s).

Optical measurements

Linear and nonlinear optical absorption measurements were conducted on a thin film sample of $W_2TiC_2T_x$ MXene. The thin film samples were prepared via spin coating (Laurell WS 400BZ-

6NPP/Lite spin coater) of ~ 2 mg/ml $W_2TiC_2T_x$ MXene solution on a fused silica substrate. Before spin coating, the fused silica substrates were plasma etched (PE-50 Compact Benchtop Plasma Cleaning System) for 30 seconds. The thin film samples were prepared using single-step spin coating at 800 RPM for 60 seconds and were vacuum-dried before optical measurements. For optical absorption data, the first transmission of the sample (T_{sample}) and a bare substrate ($T_{substrate}$) was found using the RC2 ellipsometer system made by J.A. Woolam company. The absorbance was calculated using the formula $A = -Log(T_{sample}/T_{substrate})$.

Nonlinear transmission data was found using an I-scan technique [88] where a calibrated silicon photodiode measured the transmitted power as the incident power increased. An 800 nm pulsed Q-switched femtosecond laser with a pulse width of 100 fs and a repetition rate of 1 kHz was used. Additionally, to mitigate thermal effects, a shutter opened for each measurement, only allowing for approximately 5 pulses to be incident on the sample. For each incident power, 80 measurements were averaged together. The I-scan was automated to minimize any external influence. Additionally, multiple reference measurements through the course of the I-scan at the lowest incident power determined no material damage occurred. For the calculation of fluence, the beam width was measured to be about 150 µm using a knife-edge experiment.

Raman spectral measurements

Raman spectral measurements were performed using an alpha300R Witec Spectral imaging system with 1 mW of 532 nm laser light focused to an approximately diffraction-limited spot size of 360 nm with a 100X/0.95 NA objective in a backscattering arrangement. Scattered light was dispersed with a Czerny-Turner spectrometer using a 300 l/mm grating resulting in a spectral accuracy of <1.5 cm^{-1}. Average spectra were obtained that were representative of a given sample.

Acknowledgements

References

1.   Chu S, Cui Y, Liu N. The path towards sustainable energy. *Nature materials* 2017, **16**(1)**:** 16-22.

2.   Roger I, Shipman MA, Symes MD. Earth-abundant catalysts for electrochemical and photoelectrochemical water splitting. *Nature Reviews Chemistry* 2017, **1**(1)**:** 0003.

3.   Steele BC, Heinzel A. Materials for fuel-cell technologies. *Nature* 2001, **414**(6861)**:** 345-352.

4.   Thakur A, Ghosh D, Devi P, Kim K-H, Kumar P. Current progress and challenges in photoelectrode materials for the production of hydrogen. *Chemical Engineering Journal* 2020, **397:** 125415.

5.   Wang T, Xie H, Chen M, D'Aloia A, Cho J, Wu G*, et al.* Precious metal-free approach to hydrogen electrocatalysis for energy conversion: From mechanism understanding to catalyst design. *Nano Energy* 2017, **42:** 69-89.

6.   Seh ZW, Kibsgaard J, Dickens CF, Chorkendorff I, Nørskov JK, Jaramillo TF. Combining theory and experiment in electrocatalysis: Insights into materials design. *Science* 2017, **355**(6321)**:** eaad4998.

7.   Fleischer M. *Recent estimates of the abundances of the elements in the earth's crust*, vol. 285. US Department of the Interior, Geological Survey, 1953.

8.   Energy USDo. Critical Materials and Critical Minerals.   2023   [cited]Available from: https://www.energy.gov/cmm/what-are-critical-materials-and-critical-minerals

9.   Harnisch F, Sievers G, Schröder U. Tungsten carbide as electrocatalyst for the hydrogen evolution reaction in pH neutral electrolyte solutions. *Applied Catalysis B: Environmental* 2009, **89**(3-4)**:** 455-458.

10.   Wondimu TH, Bayeh AW, Kabtamu DM, Xu Q, Leung P, Shah AA. Recent progress on tungsten oxide-based materials for the hydrogen and oxygen evolution reactions. *International Journal of Hydrogen Energy* 2022.

11.   Cui Y, Tan X, Xiao K, Zhao S, Bedford NM, Liu Y*, et al.* Tungsten oxide/carbide surface heterojunction catalyst with high hydrogen evolution activity. *ACS Energy Letters* 2020, **5**(11)**:** 3560-3568.

12.   Shi J, Pu Z, Liu Q, Asiri AM, Hu J, Sun X. Tungsten nitride nanorods array grown on carbon cloth as an efficient hydrogen evolution cathode at all pH values. *Electrochimica Acta* 2015, **154:** 345-351.

13.   Chang C, Xie Y, Luo F, Zhou S, Yang Z. Weakening sd orbital hybridization of metallic iridium by tungsten atoms for acidic water splitting. *Applied Catalysis A: General* 2023, **649:** 118941.

14.   Han N, Yang KR, Lu Z, Li Y, Xu W, Gao T*, et al.* Nitrogen-doped tungsten carbide nanoarray as an efficient bifunctional electrocatalyst for water splitting in acid. *Nature communications* 2018, **9**(1)**:** 924.

15.   Zhang D, Wang F, Zhao W, Cui M, Fan X, Liang R, *et al.* Boosting Hydrogen Evolution Reaction Activity of Amorphous Molybdenum Sulfide Under High Currents Via Preferential Electron Filling Induced by Tungsten Doping. *Advanced Science* 2022, **9**(27)**:** 2202445.

16.   Kou Z, Wang T, Wu H, Zheng L, Mu S, Pan Z, *et al.* Twinned tungsten carbonitride nanocrystals boost hydrogen evolution activity and stability. *Small* 2019, **15**(19)**:** 1900248.

17.   Shi M, Li W, Fang J, Jiang Z, Gao J, Chen Z, *et al.* Electronic structure tuning during facile construction of two-phase tungsten based electrocatalyst for hydrogen evolution reaction. *Electrochimica Acta* 2018, **283:** 834-841.

18.   Xu W, Ni XM, Zhang LJ, Yang F, Peng Z, Huang YF, *et al.* Tuning the electronic structure of tungsten oxide for enhanced hydrogen evolution reaction in alkaline electrolyte. *ChemElectroChem* 2022, **9**(5)**:** e202101300.

19.   Antolini E, Gonzalez ER. Tungsten-based materials for fuel cell applications. *Applied Catalysis B: Environmental* 2010, **96**(3-4)**:** 245-266.

20.   Huang H, Hu G, Hu C, Fan X. Enhanced Hydrogen Evolution Reactivity of T'-Phase Tungsten Dichalcogenides (WS_2, WSe_2, and WTe_2) Materials: A DFT Study. *International Journal of Molecular Sciences* 2022, **23**(19)**:** 11727.

21.   Voiry D, Yamaguchi H, Li J, Silva R, Alves DC, Fujita T, *et al.* Enhanced catalytic activity in strained chemically exfoliated WS_2 nanosheets for hydrogen evolution. *Nature materials* 2013, **12**(9)**:** 850-855.

22.   Wang Z, Wu HH, Li Q, Besenbacher F, Li Y, Zeng XC, *et al.* Reversing interfacial catalysis of ambipolar WSe_2 single crystal. *Advanced Science* 2020, **7**(3)**:** 1901382.

23.   Wang X, Wang J, Wei B, Zhang N, Xu J, Miao H, *et al.* Plasma tailoring in WTe_2 nanosheets for efficiently boosting hydrogen evolution reaction. *Journal of Materials Science & Technology* 2021, **78:** 170-175.

24.   Li Z, Wu Y. 2D Early Transition Metal Carbides (MXenes) for Catalysis. *Small* 2019, **15**(29)**:** 1804736.

25.   Zhong Q, Li Y, Zhang G. Two-dimensional MXene-based and MXene-derived photocatalysts: Recent developments and perspectives. *Chemical Engineering Journal* 2021, **409:** 128099.

26.   Seh ZW, Fredrickson KD, Anasori B, Kibsgaard J, Strickler AL, Lukatskaya MR, *et al.* Two-dimensional molybdenum carbide (MXene) as an efficient electrocatalyst for hydrogen evolution. *ACS Energy Letters* 2016, **1**(3)**:** 589-594.

27.   Li X, Huang Z, Shuck CE, Liang G, Gogotsi Y, Zhi C. MXene chemistry, electrochemistry and energy storage applications. *Nature Reviews Chemistry* 2022, **6**(6)**:** 389-404.

28.   Lim KRG, Shekhirev M, Wyatt BC, Anasori B, Gogotsi Y, Seh ZW. Fundamentals of MXene synthesis. *Nature Synthesis* 2022**:** 1-14.

29.   Wyatt BC, Rosenkranz A, Anasori B. 2D MXenes: Tunable Mechanical and Tribological Properties. *Adv Mater* 2021, **33**(17)**:** 2007973.

30.   Hart JL, Hantanasirisakul K, Lang AC, Li Y, Mehmood F, Pachter R*, et al.* Multimodal Spectroscopic Study of Surface Termination Evolution in $Cr_2TiC_2T_x$ MXene. *Advanced Materials Interfaces* 2021, **8**(5)**:** 2001789.

31.   Zeraati AS, Mirkhani SA, Sun P, Naguib M, Braun PV, Sundararaj U. Improved synthesis of $Ti_3C_2T_x$ MXenes resulting in exceptional electrical conductivity, high synthesis yield, and enhanced capacitance. *Nanoscale* 2021, **13**(6)**:** 3572-3580.

32.   Lipatov A, Alhabeb M, Lu H, Zhao S, Loes MJ, Vorobeva NS*, et al.* Electrical and Elastic Properties of Individual Single-Layer $Nb_4C_3T_x$ MXene Flakes. *Advanced Electronic Materials* 2020, **6**(4)**:** 1901382.

33.   Li X, Wang C, Cao Y, Wang G. Functional MXene Materials: Progress of Their Applications. *Chemistry – An Asian Journal* 2018, **13**(19)**:** 2742-2757.

34.   Lim KRG, Handoko AD, Nemani SK, Wyatt B, Jiang H-Y, Tang J*, et al.* Rational Design of Two-Dimensional Transition Metal Carbide/Nitride (MXene) Hybrids and Nanocomposites for Catalytic Energy Storage and Conversion. *ACS Nano* 2020, **14**(9)**:** 10834-10864.

35.   Li Z, Wang L, Sun D, Zhang Y, Liu B, Hu Q*, et al.* Synthesis and thermal stability of two-dimensional carbide MXene Ti_3C_2. *Materials Science and Engineering: B* 2015, **191:** 33-40.

36.   Pinto D, Anasori B, Avireddy H, Shuck CE, Hantanasirisakul K, Deysher G*, et al.* Synthesis and electrochemical properties of 2D molybdenum vanadium carbides – solid solution MXenes. *Journal of Materials Chemistry A* 2020, **8**(18)**:** 8957-8968.

37.   Anasori B, Lukatskaya MR, Gogotsi Y. 2D metal carbides and nitrides (MXenes) for energy storage. *Nat Rev Mater* 2017, **2**(2)**:** 16098.

38.   Naguib M, Mochalin VN, Barsoum MW, Gogotsi Y. 25th Anniversary Article: MXenes: A New Family of Two-Dimensional Materials. *Advanced Materials* 2014, **26**(7)**:** 992-1005.

39.   VahidMohammadi A, Rosen J, Gogotsi Y. The world of two-dimensional carbides and nitrides (MXenes). *Science* 2021, **372**(6547)**:** eabf1581.

40.   Sokol M, Natu V, Kota S, Barsoum MW. On the Chemical Diversity of the MAX Phases. *Trends in Chemistry* 2019, **1**(2)**:** 210-223.

41.   Naguib M, Kurtoglu M, Presser V, Lu J, Niu J, Heon M*, et al.* Two-dimensional nanocrystals produced by exfoliation of Ti_3AlC_2. *Advanced Materials* 2011, **23**(37)**:** 4248-4253.

42.   Mathis TS, Maleski K, Goad A, Sarycheva A, Anayee M, Foucher AC*, et al.* Modified MAX Phase Synthesis for Environmentally Stable and Highly Conductive Ti_3C_2 MXene. *ACS Nano* 2021, **15**(4)**:** 6420-6429.

43. Wang X, Garnero C, Rochard G, Magne D, Morisset S, Hurand S, *et al.* A new etching environment (FeF$_3$/HCl) for the synthesis of two-dimensional titanium carbide MXenes: a route towards selective reactivity vs. water. *Journal of Materials Chemistry A* 2017, **5**(41)**:** 22012-22023.

44. Liu F, Zhou A, Chen J, Jia J, Zhou W, Wang L*, et al.* Preparation of Ti$_3$C$_2$ and Ti$_2$C MXenes by fluoride salts etching and methane adsorptive properties. *Applied Surface Science* 2017, **416:** 781-789.

45. Liu L, Orbay M, Luo S, Duluard S, Shao H, Harmel J*, et al.* Exfoliation and Delamination of Ti$_3$C$_2$T$_x$ MXene Prepared via Molten Salt Etching Route. *ACS nano* 2021, **16**(1)**:** 111-118.

46. Li T, Yao L, Liu Q, Gu J, Luo R, Li J*, et al.* Fluorine-free synthesis of high-purity Ti$_3$C$_2$T$_x$ (T= OH, O) via alkali treatment. *Angewandte Chemie International Edition* 2018, **57**(21)**:** 6115-6119.

47. Chen J, Chen M, Zhou W, Xu X, Liu B, Zhang W*, et al.* Simplified Synthesis of Fluoride-Free Ti$_3$C$_2$T$_x$ via Electrochemical Etching toward High-Performance Electrochemical Capacitors. *ACS nano* 2022, **16**(2)**:** 2461-2470.

48. Shuck CE, Gogotsi Y. Taking MXenes from the lab to commercial products. *Chemical Engineering Journal* 2020, **401:** 125786.

49. Shuck CE, Sarycheva A, Anayee M, Levitt A, Zhu Y, Uzun S*, et al.* Scalable Synthesis of Ti$_3$C$_2$T$_x$ MXene. *Advanced Engineering Materials* 2020, **22**(3)**:** 1901241.

50. Wu J, Su J, Wu T, Huang L, Li Q, Luo Y*, et al.* Scalable Synthesis of 2D Mo$_2$C and Thickness-Dependent Hydrogen Evolution on Its Basal Plane and Edges. 2023**:** 2209954.

51. Meshkian R, Dahlqvist M, Lu J, Wickman B, Halim J, Thörnberg J*, et al.* W-Based Atomic Laminates and Their 2D Derivative W$_{1.33}$C MXene with Vacancy Ordering. *Advanced Materials* 2018, **30**(21)**:** 1706409.

52. Handoko AD, Fredrickson KD, Anasori B, Convey KW, Johnson LR, Gogotsi Y*, et al.* Tuning the basal plane functionalization of two-dimensional metal carbides (MXenes) to control hydrogen evolution activity. *ACS Applied Energy Materials* 2017, **1**(1)**:** 173-180.

53. Jin D, Johnson LR, Raman AS, Ming X, Gao Y, Du F*, et al.* Computational screening of 2D ordered double transition-metal carbides (MXenes) as electrocatalysts for hydrogen evolution reaction. *The Journal of Physical Chemistry C* 2020, **124**(19)**:** 10584-10592.

54. Pan H. Ultra-high electrochemical catalytic activity of MXenes. *Scientific reports* 2016, **6**(1)**:** 32531.

55. Lei J-C, Zhang X, Zhou Z. Recent advances in MXene: Preparation, properties, and applications. *Front Phys-Beijing* 2015, **10**(3)**:** 276-286.

56. Khaledialidusti R, Khazaei M, Khazaei S, Ohno K. High-throughput computational discovery of ternary-layered MAX phases and prediction of their exfoliation for formation of 2D MXenes. *Nanoscale* 2021, **13**(15)**:** 7294-7307.

57. Lind H, Wickman B, Halim J, Montserrat-Sisó G, Hellman A, Rosen JJASS. Hydrogen evolution reaction for vacancy-ordered i-MXenes and the impact of proton absorption into the vacancies. 2021, **5**(2)**:** 2000158.

58. Dahlqvist M, Rosen JJPCCP. Order and disorder in quaternary atomic laminates from first-principles calculations. 2015, **17**(47)**:** 31810-31821.

59. Dahlqvist M, Rosen JJN. Predictive theoretical screening of phase stability for chemical order and disorder in quaternary 312 and 413 MAX phases. 2020, **12**(2)**:** 785-794.

60. Anasori B, Lu J, Rivin O, Dahlqvist M, Halim J, Voigt C*, et al.* A Tungsten-Based Nanolaminated Ternary Carbide: (W,Ti)$_4$C$_{4-x}$. *Inorganic Chemistry* 2019, **58**(2)**:** 1100-1106.

61. Michałowski PP, Anayee M, Mathis TS, Kozdra S, Wójcik A, Hantanasirisakul K*, et al.* Oxycarbide MXenes and MAX phases identification using monoatomic layer-by-layer analysis with ultralow-energy secondary-ion mass spectrometry. *Nature Nanotechnology* 2022, **17**(11)**:** 1192-1197.

62. Zhang D, Shah D, Boltasseva A, Gogotsi Y. MXenes for Photonics. *ACS Photonics* 2022, **9**(4)**:** 1108-1116.

63. Simon J, Fruhling C, Kim H, Gogotsi Y, Boltasseva A. MXenes for Optics and Photonics. *Optics and Photonics News* 2023, **34**(11)**:** 42-49.

64. Anasori B, Shi C, Moon EJ, Xie Y, Voigt CA, Kent PR*, et al.* Control of electronic properties of 2D carbides (MXenes) by manipulating their transition metal layers. 2016, **1**(3)**:** 227-234.

65. Thakur A, Chandran BS N, Davidson K, Bedford A, Fang H, Im Y*, et al.* Step-by-Step Guide for Synthesis and Delamination of Ti$_3$C$_2$T$_x$ MXene. *Small Methods* 2023**:** 2300030.

66. Shekhirev M, Shuck CE, Sarycheva A, Gogotsi YJPiMS. Characterization of MXenes at every step, from their precursors to single flakes and assembled films. 2021, **120:** 100757.

67. Alhabeb M, Maleski K, Anasori B, Lelyukh P, Clark L, Sin S*, et al.* Guidelines for Synthesis and Processing of Two-Dimensional Titanium Carbide (Ti$_3$C$_2$T$_x$ MXene). *Chemistry of Materials* 2017, **29**(18)**:** 7633-7644.

68. Michałowski PP, Anayee M, Mathis TS, Kozdra S, Wójcik A, Hantanasirisakul K*, et al.* Oxycarbide MXenes and MAX phases identification using monoatomic layer-by-layer analysis with ultralow-energy secondary-ion mass spectrometry. *Nature Nanotechnology* 2022, **17**(11)**:** 1192-1197.

69. Jung H, Hwang J, Chun H, Han BJJoI, Chemistry E. Elucidation of hydrolysis reaction mechanism of tungsten hexafluoride (WF6) using first-principles calculations. 2019, **70:** 99-102.

70. Atherton MJ. *Chalcogenide fluorides of molybdenum (VI) and tungsten (VI)*. University of Leicester (United Kingdom), 1977.

71. Shekhirev M, Shuck CE, Sarycheva A, Gogotsi Y. Characterization of MXenes at every step, from their precursors to single flakes and assembled films. *Progress in Materials Science* 2021, **120:** 100757.

72. Badr HO, Cope J, Kono T, Torita T, Lagunas F, Castiel E*, et al.* Titanium oxide-based 1D nanofilaments, 2D sheets, and mesoporous particles: Synthesis, characterization, and ion intercalation. *Matter* 2023, **6**(10)**:** 3538-3554.

73. Sarycheva A, Gogotsi Y. Raman spectroscopy analysis of the structure and surface chemistry of $Ti_3C_2T_x$ MXene. *Chemistry of Materials* 2020, **32**(8)**:** 3480-3488.

74. Shevchuk K, Sarycheva A, Shuck CE, Gogotsi Y. Raman Spectroscopy Characterization of 2D Carbide and Carbonitride MXenes. *Chemistry of Materials* 2023, **35**(19)**:** 8239-8247.

75. Badr HO, Montazeri K, El-Melegy T, Natu V, Carey M, Gawas R*, et al.* Scalable, inexpensive, one-pot, facile synthesis of crystalline two-dimensional birnessite flakes. *Matter* 2022, **5**(7)**:** 2365-2381.

76. Badr HO, El-Melegy T, Carey M, Natu V, Hassig MQ, Johnson C*, et al.* Bottom-up, scalable synthesis of anatase nanofilament-based two-dimensional titanium carbo-oxide flakes. *Materials Today* 2022, **54:** 8-17.

77. Colin-Ulloa E, Martin JL, Hanna RJ, Frasch MH, Ramthun RR, Badr HO*, et al.* Electronic Structure of 1D Lepidocrocite TiO2 as Revealed by Optical Absorption and Photoelectron Spectroscopy. *The Journal of Physical Chemistry C* 2023.

78. Halim J. *An X-ray Photoelectron spectroscopy study of multilayered transition metal carbides (MXenes)*. Drexel University, 2016.

79. Halim J, Cook KM, Eklund P, Rosen J, Barsoum MW. XPS of cold pressed multilayered and freestanding delaminated 2D thin films of $Mo_2TiC_2T_z$ and $Mo_2Ti_2C_3T_z$ (MXenes). *Applied Surface Science* 2019, **494:** 1138-1147.

80. Xu JY, Elangovan A, Li J, Liu B. Graphene-Based Dual-Metal Sites for Oxygen Reduction Reaction: A Theoretical Study. *J Phys Chem C* 2021, **125**(4)**:** 2334-2344.

81. Norskov JK, Rossmeisl J, Logadottir A, Lindqvist L, Kitchin JR, Bligaard T*, et al.* Origin of the overpotential for oxygen reduction at a fuel-cell cathode. *J Phys Chem B* 2004, **108**(46)**:** 17886-17892.

82. Norskov JK, Abild-Pedersen F, Studt F, Bligaard T. Density functional theory in surface chemistry and catalysis. *Proc Natl Acad Sci U S A* 2011, **108**(3)**:** 937-943.

83. Brian C. Wyatt AT, Kat Nykiel, Zachary D. Hood, Shiba P. Adhikari, Krista K. Pulley, Wyatt J. Highland, Alejandro Strachan, and Babak Anasori. Design of Atomic Ordering in $Mo_2Nb_2C_3T_x$ MXenes for Hydrogen Evolution Electrocatalysis. 2023.

84. Urbankowski P, Anasori B, Hantanasirisakul K, Yang L, Zhang L, Haines B*, et al.* 2D molybdenum and vanadium nitrides synthesized by ammoniation of 2D transition metal carbides (MXenes). *Nanoscale* 2017, **9**(45)**:** 17722-17730.

85. Halim J, Moon EJ, Eklund P, Rosen J, Barsoum MW, Ouisse T. Variable range hopping and thermally activated transport in molybdenum-based MXenes. *Phys Rev B* 2018, **98**(10)**:** 104202.

86. Éfros AL, Shklovskii BI. Coulomb gap and low temperature conductivity of disordered systems. *Journal of Physics C: Solid State Physics* 1975, **8**(4)**:** L49.

87. Maleski K, Shuck CE, Fafarman AT, Gogotsi Y. The Broad Chromatic Range of Two-Dimensional Transition Metal Carbides. *Advanced Optical Materials* 2021, **9**(4)**:** 2001563.

88. Taheri B, Liu H, Jassemnejad B, Appling D, Powell RC, Song JJ. Intensity scan and two photon absorption and nonlinear refraction of C60 in toluene. *Applied Physics Letters* 1996, **68**(10)**:** 1317-1319.

89. Menzel R. *Photonics: linear and nonlinear interactions of laser light and matter.* Springer Science & Business Media, 2013.

90. Kresse G, Furthmuller J. Efficient iterative schemes for ab initio total-energy calculations using a plane-wave basis set. *Phys Rev B* 1996, **54**(16)**:** 11169-11186.

91. Kresse G, Furthmüller J. Efficiency of ab-initio total energy calculations for metals and semiconductors using a plane-wave basis set. *Comp Mater Sci* 1996, **6**(1)**:** 15-50.

92. Perdew JP, Burke K, Ernzerhof M. Generalized gradient approximation made simple. *Phys Rev Lett* 1996, **77**(18)**:** 3865-3868.

93. Monkhorst HJ, Pack JD. Special Points for Brillouin-Zone Integrations. *Phys Rev B* 1976, **13**(12)**:** 5188-5192.

94. Grimme S. Semiempirical GGA-type density functional constructed with a long-range dispersion correction. *Journal of Computational Chemistry* 2006, **27**(15)**:** 1787-1799.

95. Xu J, Liu B. Intrinsic properties of nitrogen-rich carbon nitride for oxygen reduction reaction. *Appl Surf Sci* 2020, **500:** 144020.

96. Li N, Chen XZ, Ong WJ, MacFarlane DR, Zhao XJ, Cheetham AK*, et al.* Understanding of Electrochemical Mechanisms for CO_2 Capture and Conversion into Hydrocarbon Fuels in Transition-Metal Carbides (MXenes). *Acs Nano* 2017, **11**(11)**:** 10825-10833.

97. Li X, Dai Y, Ma Y, Han S, Huang B. Graphene/g-C_3N_4 bilayer: considerable band gap opening and effective band structure engineering. *Physical Chemistry Chemical Physics* 2014, **16**(9)**:** 4230-4235.

98.   Gan L-Y, Zhao Y-J, Huang D, Schwingenschlögl U. First-principles analysis of MoS_2/Ti_2C and MoS_2/Ti_2C_y (Y=F and OH) all-2D semiconductor/metal contacts. *Physical Review B* 2013, **87**(24)**:** 245307.

99.   Abghoui Y, Skulason E. Hydrogen Evolution Reaction Catalyzed by Transition-Metal Nitrides. *J Phys Chem C* 2017, **121**(43)**:** 24036-24045.

100.   Shan N, Zhou M, Hanchett MK, Chen J, Liu B. Practical principles of density functional theory for catalytic reaction simulations on metal surfaces – from theory to applications. *Mol Simulat* 2017, **43**(10-11)**:** 861-885.